Nanotubular Array Solid Oxide Fuel Cell

Munekazu Motoyama,[†,§,*] Cheng-Chieh Chao,[†] Jihwan An,[†] Hee Joon Jung,[‡] Turgut M. Gür,[‡] and Friedrich B. Prinz[†,‡]

[†]Department of Mechanical Engineering and [‡]Department of Materials Science & Engineering, Stanford University, Stanford, California 94305, United States.
[§]Present address: Nagoya Universisty, Furo-cho, Chikusa-ku, Nagoya, Aichi 464-8603, Japan.

ABSTRACT This report presents a demonstration and characterization of a nanotubular array of solid oxide fuel cells (SOFCs) made of one-end-closed hollow tube Ni/yttria-stabilized zirconia/Pt membrane electrode assemblies (MEAs). The tubular MEAs are nominally ~5 μm long and have <500 nm outside diameter with total MEA thickness of nearly 50 nm. Open circuit voltages up to 660 mV (*vs* air) and power densities up to 1.3 μW cm^{-2} were measured at 550 °C using H_2 as fuel. The paper also introduces a fabrication methodology primarily based on a template process involving atomic layer deposition and electrodeposition for building the nanotubular MEA architecture as an important step toward achieving high surface area ultrathin SOFCs operating in the intermediate to low-temperature regime. A fabricated nanotubular SOFC theoretically attains a 20-fold increase in the effective surface, while projections indicate the possibility of achieving up to 40-fold.

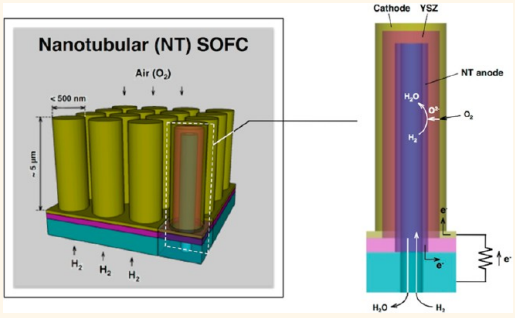

KEYWORDS: electrodeposition · porous template · nanostructured MEA · atomic layer deposition · solid oxide fuel cell

Fabrication of ultrathin (~50 nm) nanotubular (NT) solid oxide fuel cells (SOFC) is successfully demonstrated in this study. This accomplishment constitutes an important step toward reducing the cell operating temperature to below 600 °C, which also helps reduce material costs and stability requirements for SOFCs.

SOFC is an efficient electrochemical engine that converts the chemical energy stored in the chemical bonds of fuels directly into electrical energy. SOFCs offer several advantages in comparison to other types of fuel cells. (1) SOFCs offer fuel flexibility as well as fast kinetic and transport rates. (2) There is no concern about water management or methanol crossover, which are difficult problems in polymer electrolyte membrane fuel cells (PEMFC) and direct methanol fuel cells (DMFC), respectively. (3) Non-Pt catalysts can be employed for operation even at intermediate temperatures. (4) Theoretical conversion efficiency is typically higher than for other types of fuel cells. (5) SOFCs generate high-quality waste heat that can further be used in a combined heat and power (CHP) system for improved efficiency. (6) Entirely solid-state components offer a wider range of choices for cell geometries including tubular or planar SOFCs.

To make NT-SOFCs, we have employed a nanoporous template. This method was demonstrated previously to produce vertical arrays of one-dimensional (1-D) nanostructures such as nanowires (NWs) or NTs.[1,2] These high-aspect-ratio 1-D nanostructure arrays have large specific surface areas. Furthermore, they offer several benefits for energy conversion devices in comparison to random porous supports.[3−9] First, the entire surface, including the side walls of the nanostructured array, is accessible from top free space (*i.e.*, the gas phase), whereby modifying the surfaces with, for example, catalytic particles can be achieved effectively. Moreover, this geometric feature is beneficial for chemical reactants to reach all available surfaces of the nanostructured arrays, while the products can diffuse out quickly. More importantly, the NT geometry minimizes diffusion distances. Therefore, efficient charge transport can be achieved by virtue of straight and short paths in such 1-D-oriented nanostructures.

The present study builds upon our earlier work, where we have already demonstrated

* Address correspondence to munekazu@numse.nagoya-u.ac.jp.

Received for review August 13, 2013 and accepted November 22, 2013.

Published online November 22, 2013
10.1021/nn4042305

successful fabrication of self-standing micro-SOFCs on silicon wafers employing ~100 nm thin solid oxide electrolyte films made by atomic layer deposition (ALD).[10−12]

ALD is, in principle, a layer-by-layer, surface-reaction-limited thin film deposition technique relying on sterically hindered adsorption of organometallic gaseous precursors that quickly diffuse on the substrate surface to form monolayers. Hence, thin film growth occurs conformally everywhere on the substrate in ALD regardless of its geometry. ALD's ability to coat a conformal thin electrolyte film on nonflat or even complex geometry substrates provides a large degree of freedom in cell design.

The ultrathin (~100 nm) yttria-stabilized zirconia (YSZ) films previously fabricated by ALD in our laboratory significantly helped reduce electrolyte resistance and enhanced cell performance.[10−12] Also, Su *et al.* employed substrates with periodic corrugations at the micrometer scale made by MEMS micromachining such that effective surface areas per unit projected area were increased by 2−5-fold.[11] Chao *et al.* developed more finely corrugated ALD platforms using nanosphere lithographic technique and achieved power densities more than 1 W cm^{-2} at 500 °C.[12] So, the concept of increasing specific surface area by 3-D surfaces to improve fuel cell performance has therefore been successfully demonstrated by our group.

The present study demonstrates a major improvement beyond the several fold increase reported earlier for corrugated structures and achieves significantly higher aspect ratios in NT geometry that results in 20-fold increase in the specific surface area determined in the calculation. The NT geometry with ultrathin MEAs affords reduced diameters that minimize transport pathways and longer tube arrays that can be densely aligned to achieve high specific area, both of which are expected to lead to better cell performance.

High-aspect-ratio 1-D nanostructure arrays are fascinating geometries for energy conversion devices. Previous studies reported the use of electrodeposited metal NW arrays for high specific surface area electrodes.[3−9] However, there has been no report to date that has successfully integrated fully built electrode−electrolyte−electrode assemblies (MEA) in a free-standing 1-D nanoarchitectured fuel cells (Figure 1). The aim of the present study is to develop the ability and introduce the methodology to fabricate ALD-based high surface area NT-SOFC architecture toward fuel cell miniaturization through the use of vertically aligned 1-D nanostructures as depicted in Figure 1. We assigned the inner tube electrode for the H_2 oxidation reaction (*i.e.*, anode) since this is a facile reaction, while the overall reaction rate of SOFC is usually limited by the sluggish kinetics of O_2 reduction reaction. Hence, H_2 flow is supplied to the inner cavities of NTs that are

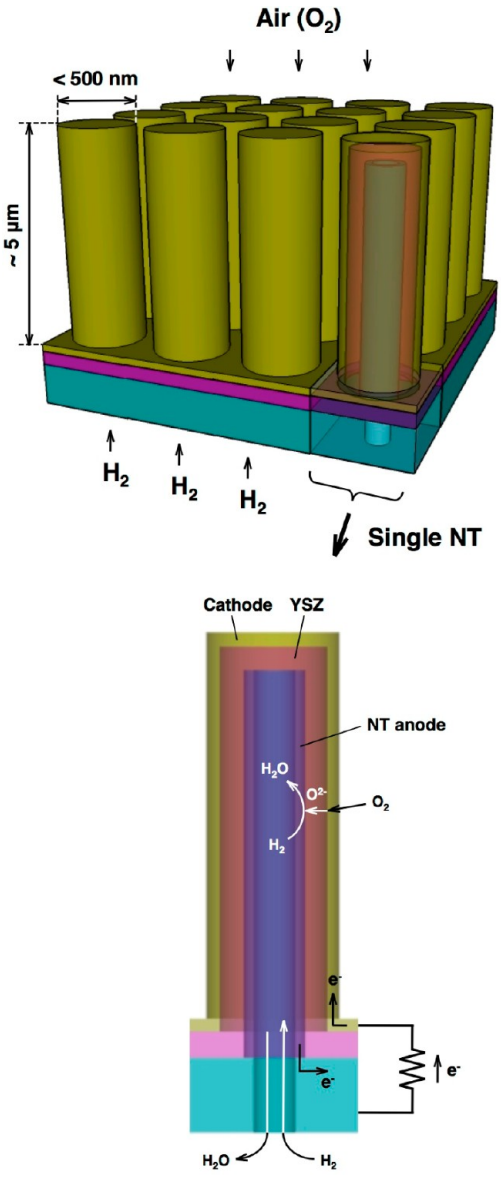

Figure 1. Conceptual schematics of a high surface area NT MEA structure for SOFC. Closed-end NTs are densely packed and vertically aligned to create high surface area for the cell electrode reactions. The right-hand-side schematic explains the role of each component and how electrons and chemical species move inside a single NT. The inner and outer walls of the NT form the anode and the cathode, respectively. The YSZ tubular annulus between the cathode and anode layers serves as the solid electrolyte. H_2 gas enters the hollow interior of the NT from the bottom opening and reacts with the oxide ions that migrate through the YSZ electrode to form H_2O. O_2 gas in air is reduced at the cathode before it is incorporated into the YSZ electrolyte. The potential difference generated across the YSZ membrane drives the electrons through the external circuit.

less accessible to gas diffusion compared to the outer sides of NTs. We also observed tolerance of the NT MEA structure to stresses that are induced by mismatches in thermal expansion coefficients. Although the NT-SOFC embodied in this work is far from being of practical use and definitely requires further development, we nevertheless hope this paper inspires advancements in the

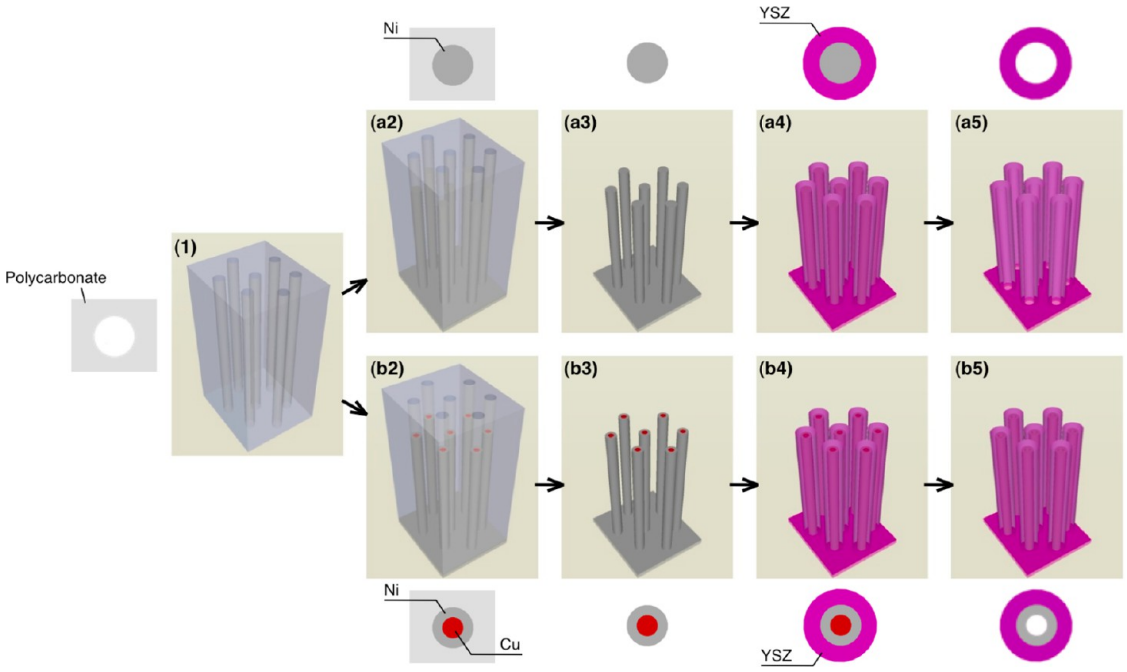

Figure 2. Process steps and schematic cross sections illustrate the two parallel fabrication pathways to make NT MEA structures. (1) Polycarbonate track-etched membrane template. (a2) Electrodeposition of Ni NWs into membrane. (a3,b3) Removal of membrane. (a4,b4) ALD of YSZ film. (a5) Chemical etching of Ni. (b2) Electrodeposition of core–shell Cu–Ni NWs into membrane. (b5) Anodic dissolution of Cu.

design of a broad range of nanostructured energy conversion devices.

The parallel sequence of process steps during fabrication of NT MEA structures is illustrated along pathways in Figure 2. A Pt–Pd alloy film of approximately 30 nm in thickness was sputter-deposited on the top surface of a track-etched polycarbonate membrane (Nomura Micro Science Co.). The nominal pore diameter and number density of tracks in the template membrane were 200 nm and 3×10^8 cm^{-2}, respectively. The membrane thickness was 10 μm. A Pt–Pd alloy film serves as a cathode for electrodepositing metal NWs into pores.

RESULTS AND DISCUSSION

Surface Area Analysis. ALD-grown YSZ film on NW surfaces naturally increases the overall diameter of each NW. Hence, surface areas of NWs become larger as the ALD thickness increases. However, laterally extending NWs finally coalesce with their neighbors upon reaching specific diameter thresholds. This is depicted in the series of images shown in Figure 3.

A scanning electron microscope (SEM) image of the porous template membrane surface used in this study is shown in Figure 3a. The pore number density shown in the SEM image is 3.3×10^8 cm^{-2}, which is consistent with the nominal track density of 3×10^8 cm^{-2} reported by the template manufacturer.

Figure 3b–d depicts cases where the diameters are varied from 117 to 971 nm, keeping the same pore locations as in Figure 3a. The diameters in (b–d)

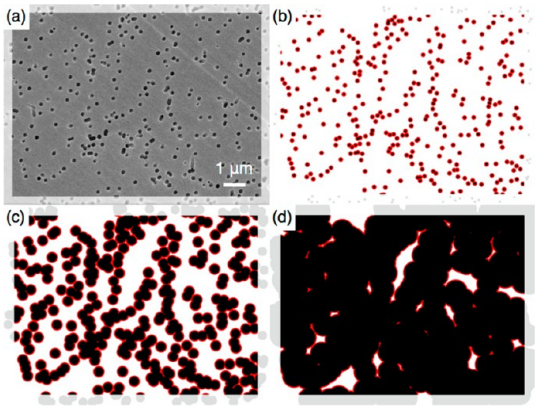

Figure 3. (a) SEM image of the polycarbonate porous membrane surface. Predicted NW cross sections based on the pore distribution in (a) are shown in (b–d). The dot diameters correspond to (b) 117 nm, (c) 418 nm, and (d) 971 nm on the same scale bar used in (a). Red peripheries of NWs are extra surfaces compared to a flat membrane.

correspond to 117, 418, and 971 nm, respectively, for the same scale bar on the SEM image in (a). If YSZ films of approximately 100 nm in thickness are deposited on NW surfaces (an overall diameter is approximately 400 nm), a top view is expected to appear as in (c). For YSZ film thickness of approximately 390 nm, lateral coalescence of NWs becomes significant as shown in (d). The fraction of the area covered by wires, θ, is greater than 0.9 in (d). The corresponding plots in Figure 4 show how θ varies as a function of diameter, d, in a series of virtual images reconstructed from Figure 3a.

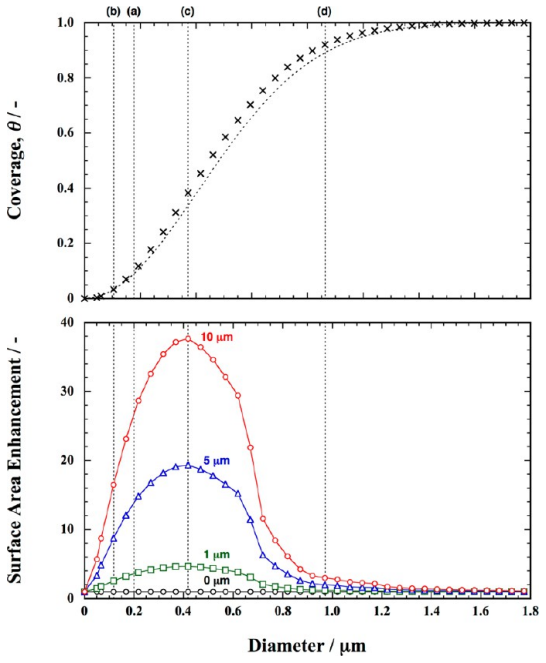

Figure 4. Overall coverage of wires, θ, and corresponding surface area enhancements with different wire heights (1, 5, 10 μm) as a function of wire diameter. The cross symbols in the top figure and the blank symbols in the bottom figure are the virtual analysis results. A dotted line is calculated by eq 1 with $N = 3 \times 10^8$ cm^{-2}. The diameters corresponding to the respective images in Figure 3 are shown in (a–d).

If θ denotes the fraction of the area covered by wires of nominal diameter d, then θ exponentially increases, resulting in full coverage (*i.e.*, $\theta = 1$) as d increases. The Avrami theorem, on the other hand, describes the general equation for θ of a number of clusters in a form of the Poisson distribution.[13,14]

$$\theta = 1 - \exp(-\theta_{ex}) \quad (1)$$

where we define θ_{ex} as

$$\theta_{ex} = \frac{N\pi d^2}{4} \quad (2)$$

Here, N is a number density of clusters. The dotted line in the top graph of Figure 4 represents the fit to the experimental values for the coverage calculated from eq 1 with $N = 3 \times 10^8$ cm^{-2}. The correspondence between the experimental values and the calculated dotted line justifies and verifies the assumption that a small section of the template surface indicated by the SEM image of Figure 3a is indeed representative of the entire template area. The surface area enhancements corresponding to respective θ values of the cross plots are also shown in Figure 4.

As shown in Figure 4, the total peripheral length reaches a maximum at a diameter of approximately 0.4 μm. In comparison to a flat substrate, the side walls of NWs are beneficial surfaces that contribute to the total surface area. Hence, d values from 0.3 to 0.5 μm can provide the largest surface area. When d is smaller than 0.4 μm, the effect of increasing surface area due to extending diameters is more significant than the effect of decreasing surface area due to coalescence of the wires. On the other hand, as wire coalescence becomes more significant, lateral surfaces of NWs decrease. Typically, the NWs have diameters of 200 nm as electrodeposited. ALD YSZ films should thus be between 50 and 150 nm in order to offer the largest surface area. In our previous work, YSZ films of 100–200 nm thickness were grown by ALD in order to optimize ionic resistance, mechanical robustness, and pinhole probability.[10] Hence, the optimum ALD thicknesses for geometric and practical reasons match well in this study. The longer the NWs are, the larger is the overall surface area. When NWs are as long as the membrane thickness of 10 μm, the overall surface area becomes almost 40 times larger than that for a flat substrate.

Fabrication of NT MEAs. Figure 5 shows the SEM top-view images of Ni NW arrays (a) as electrodeposited and (b) coated with 50 nm thick YSZ by ALD. The porous polycarbonate template membrane was removed by dissolution in dichloromethane. Free-standing NWs were obtained. After YSZ coating, NW diameters become slightly larger.

Figure 5a,b shows diameter distributions of uncoated and coated NWs, respectively. The mean diameter and standard deviation in (a) are 289 and 39 nm, respectively. This mean diameter is greater than the nominal diameter value of 200 nm. This is attributed to nonuniformity and distribution of pore diameters along the length. Pore diameters at membrane surfaces have exactly the nominal diameter as shown in Figure 3a. However, diameters tend to grow larger inside membranes. This fact has been reported by previous work and especially observed in commercial polycarbonate track-etched membranes.[15,16] The growth of NWs by electrodeposition was terminated before NWs reached the membrane surface. The tip diameters of NWs in (a) therefore are slightly greater than 200 nm.

After YSZ coating, the mean diameter and standard deviation become 393 and 44 nm, respectively, as shown in Figure 5b. This ~100 nm increase in wire diameter is double the projected ALD thickness of 50 nm. On the other hand, the standard deviation is almost the same as before ALD. These results indicate that ALD entirely coats the NW surfaces in a conformal manner.

Figure 6A shows an inverted optical microscope image of a sample with a free-standing YSZ NT array in a central square region where Ni was leached out by a HNO_3 solution. The surrounding region with Ni filled in YSZ NTs completely blocks optical light, whereas the thin free-standing YSZ NT region is translucent. The YSZ film of 200 μm × 200 μm area on the underside was removed by focused ion beam (FIB) before submerging into a HNO_3 solution. Ni NWs in the FIB-etched region were leached into a HNO_3 solution, leaving only

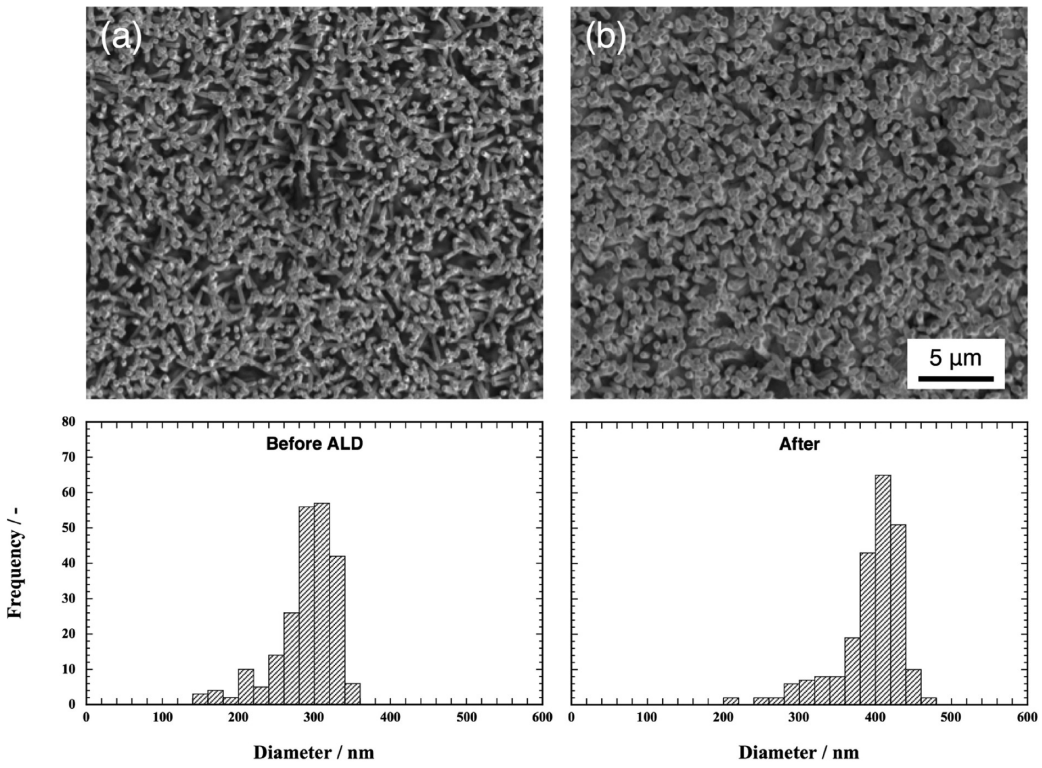

Figure 5. SEM top-view images (top) and diameter distributions (bottom) of (a) Ni NW array and (b) YSZ-coated Ni NW array. The ALD thickness is approximately 50 nm.

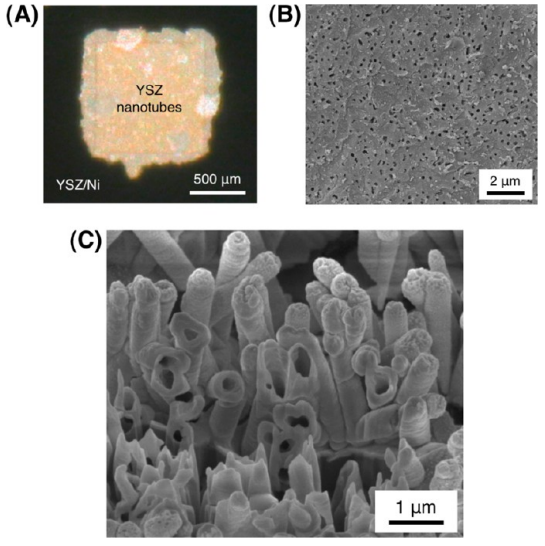

Figure 6. (A) Inverted optical microscope image of the YSZ NT array showing the area where Ni is leached out. SEM images of (B) back of the substrate and (C) tubular side with tips partly etched by FIB after chemical etching of Ni.

50 nm thick YSZ NT arrays so that the central square region appeared much brighter due to transmission of light. The dark region represents the remaining Ni NWs inside the YSZ film. Attack from the HNO_3 solution to Ni is therefore effectively slow even though the thickness of the YSZ film is only 50 nm.

Figure 6B shows the underside of a sample after being immersed in a HNO_3 solution at room temperature. Leaching of Ni from the sample creates holes as seen in Figure 6B. The number density of holes seen in Figure 6B is counted to be 3.5×10^8 cm^{-2}. This is still consistent with the nominal pore number density of 3×10^8 cm^{-2} of the template used. Selective removal of Ni NWs is achieved in a HNO_3 solution, where YSZ is stable. Hence, YSZ films remain intact, whereby hollow YSZ structures are produced after leaching out the Ni. Ultimately, 50 nm thin conformal YSZ film was deposited on the Ni NWs. The Ni was then partially leached out by HNO_3 to leave behind one-end-closed hollow YSZ tubes with a thin Ni layer to serve as the inner (fuel side) electrode for the SOFC. To assess removal of Ni from inside the YSZ NTs to allow H_2 fuel to get inside, part of the tube ends was removed using diagonal direction FIB and examined by SEM. This is shown in Figure 6C, where the hollow interiors are clearly visible in the cross-sectional images of YSZ pillars.

The cross-sectional images of Ni NWs before ALD coating with YSZ films are shown in Figure 7A. As indicated by the red arrows, small grains tend to be more observed at peripheral edges of NWs than inside their cores. On the other hand, large faceted grains are more often observed inside the cores. Figure 7B shows a cross section of partially dissolved Ni NWs inside YSZ NTs. These observations suggest that the outer peripheries of Ni NWs in contact with YSZ walls are preferentially attacked by HNO_3. This mechanism is similar to grain boundary etching, where the etchant attacks energetically unfavorable (*i.e.*, high energy)

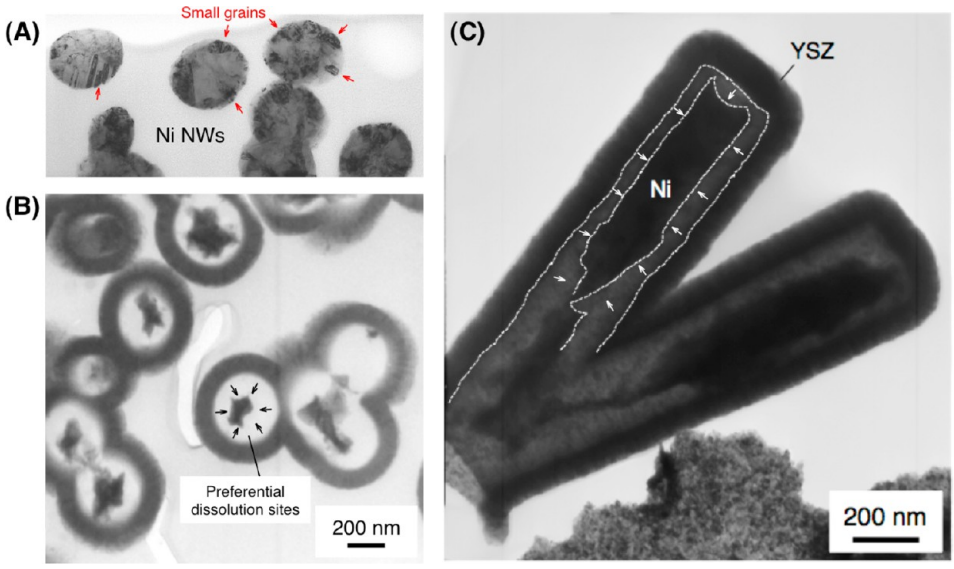

Figure 7. Cross-sectional TEM images of (A) electrodeposited Ni NWs (the red arrows indicate small grains at peripheral edges) and (B,C) YSZ NTs with partially etched Ni NWs in the hollow core.

atoms located on discontinuities or interfaces.[17] We also observed that Ni NWs inside YSZ NTs became narrower over the length (~1.5 μm) in the axial direction as shown in Figure 7C, possibly because boundaries between Ni and YSZ preferentially dissolve over the whole length. It is interesting that the remaining Ni cores inside the YSZ tubes exhibit faceted surfaces (see Figure 7B). Hence, smaller grains or ones with more defective boundaries may dissolve preferentially. The fact that chemical etching of Ni NWs gives rise to preferential leaching of interfacial regions between Ni and YSZ films makes it difficult to fabricate double-wall Ni–YSZ hollow tubes, where the adherent Ni layer can serve as the fuel electrode.

Inner Electrode Preparation. The outer peripheries of Ni NWs in contact with YSZ walls (*i.e.*, the Ni/YSZ interface) start to dissolve preferentially upon HNO_3 etching. This leads to the formation of narrow gaps at the interface between the Ni NW and the YSZ wall. The gap is clearly visible in the TEM cross-sectional image of Figure 8A. Fine crystallites of varying orientations and several nanometers in size are observed in the first 10 nm region of the YSZ wall in Figure 8B. However, as the film grows, crystallites become larger and form columnar textures in outward directions. This is attributed to film-strain energy overwhelming the surface energy after the film grows more than a certain thickness.[18] Columnar textures in ALD YSZ films were also observed previously.[10] Figure 8C,D shows cross sections of YSZ NTs where Ni is leached out. This cross-sectional picture eminently verifies the fact that the wall thickness of NTs is quite uniform in the radial direction.

To obtain an adherent inner electrode and form double-wall Ni–YSZ NT arrays, core–shell Cu–Ni NW fabrication was investigated in this study. It was previously reported that the use of aqueous solutions containing sulfamate ions ($H_2NSO_3^-$) leads to segregation of Cu and Ni in the core and peripheral regions of NWs, respectively, when Cu and Ni are co-electrodeposited.[19,20] Liu *et al.* extensively examined the effects of deposition potential and Cu^{2+} ion concentration on Cu–Ni phase separation. Their results indicate that more negative deposition potentials and higher Cu^{2+} concentrations invoke phase separation. This means that fast Cu nucleation in the initial stage of electrodeposition triggers the growth of Cu single phase. In subsequent stages, Ni growth occurs on Cu and coats the nucleated Cu islands.[20] Cu can then be electrochemically etched in the same solution while retaining a thin layer of Ni, thereby creating Ni hollow tubes.

Figure 9A shows a TEM image of Ni NTs produced by electrodeposition at −0.9 V (*vs* Ni reference electrode) followed by electrochemical etching of Cu cores at +1.0 V (*vs* Cu reference electrode). As reported in the literature,[19,20] hollow NT structures are created. Cross-sectional TEM images of the double-wall Ni–YSZ NT array shown in Figure 9B indicate that all cross sections have hollow cores. This confirms that double-layer NT walls are recognized. Sputter deposition of porous Pt was performed onto the outside surfaces of the resulting double-wall Ni–YSZ NT arrays to obtain the fully developed Ni/YSZ/Pt MEA structure.

Characterization of NT MEAs. The tubular MEAs are fully characterized for structural, microstructural, and compositional analyses. Figure 10a,b shows the SEM images of porous surface morphologies of the double-wall NTs after Pt deposition. Diameters of multi-wall Ni/YSZ/Pt NTs eventually become approximately 500 nm, which is still within the range to achieve a high specific surface area (see Figure 4). The lengths of fabricated NTs are roughly 5 μm. Accordingly, we

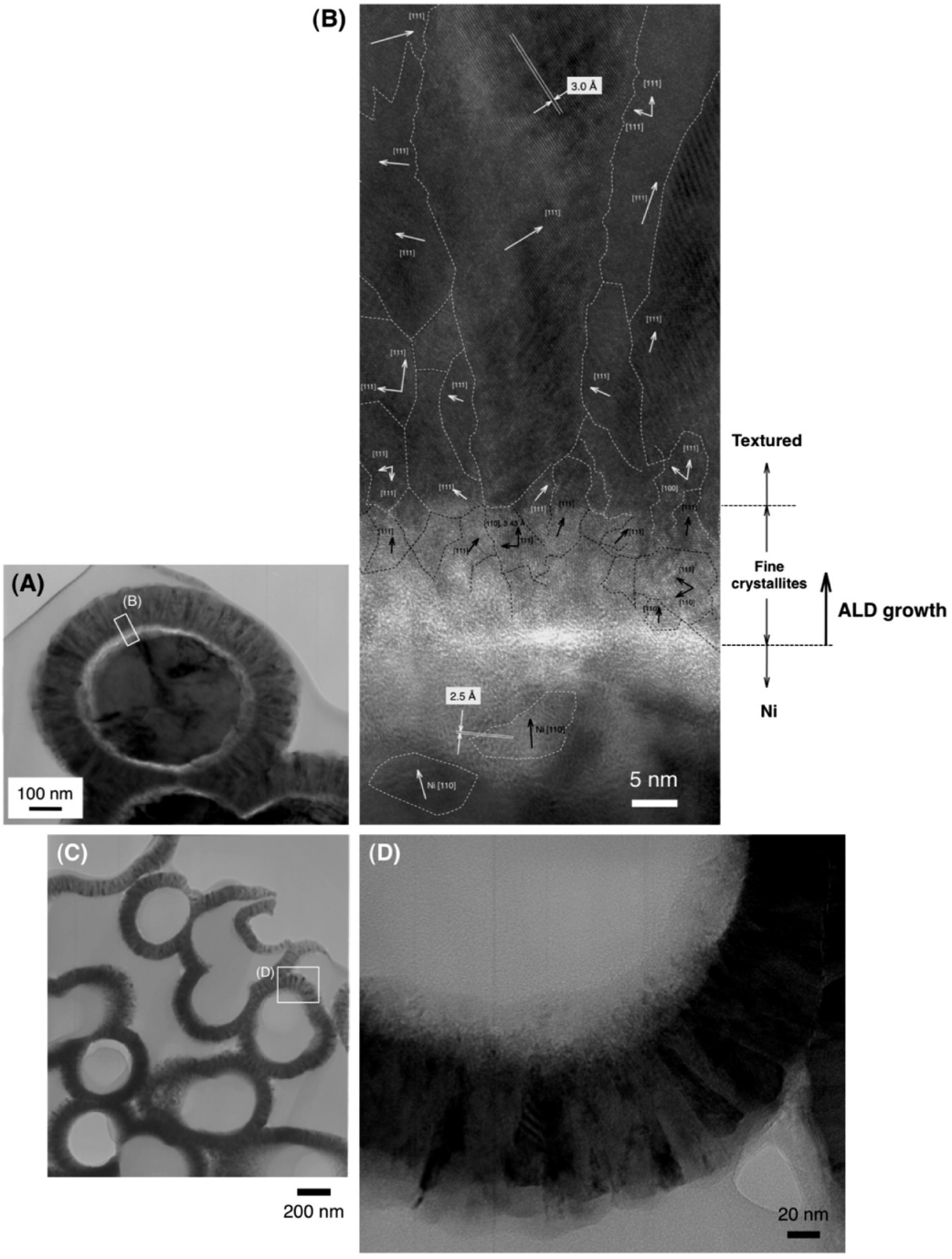

Figure 8. (A) Cross-sectional TEM image of YSZ-coated Ni NWs (slightly etched). (B) Magnified image of the square region in (A). (C) YSZ NTs. (D) Magnified image of the square region in (C).

approximate that a 20-fold increase in surface area was achieved. The cross-sectional image in the longitudinal direction of a multiwall Ni/YSZ/Pt NT is observed by TEM in Figure 10c. It is clear that the NTs have hollow interiors and porous Ni layers inside closed-end YSZ NTs. The outer and inner diameters are almost uniform over the length of the NT. The overall NT wall thickness at the tip is slightly larger than at the side walls. This is because sputtering is basically a unidirectional deposition technique so that Pt is more thickly deposited on the tip of NTs than on the vertical sides.[11] At higher magnification, the porous microstructure of the Pt film is evident (Figure 10d).

A TEM picture of YSZ NTs is also shown in Figure 11a. The tips of several tubes are seen with clear hollow structures. YSZ NT walls have uniform thicknesses of approximately 50 nm. In higher resolution images (Figure 11b), crystallites of approximately 5 nm in diameter are observed.

Figure 11c shows the energy-dispersive X-ray spectroscopy (EDS) spectra taken at positions A, B, and C

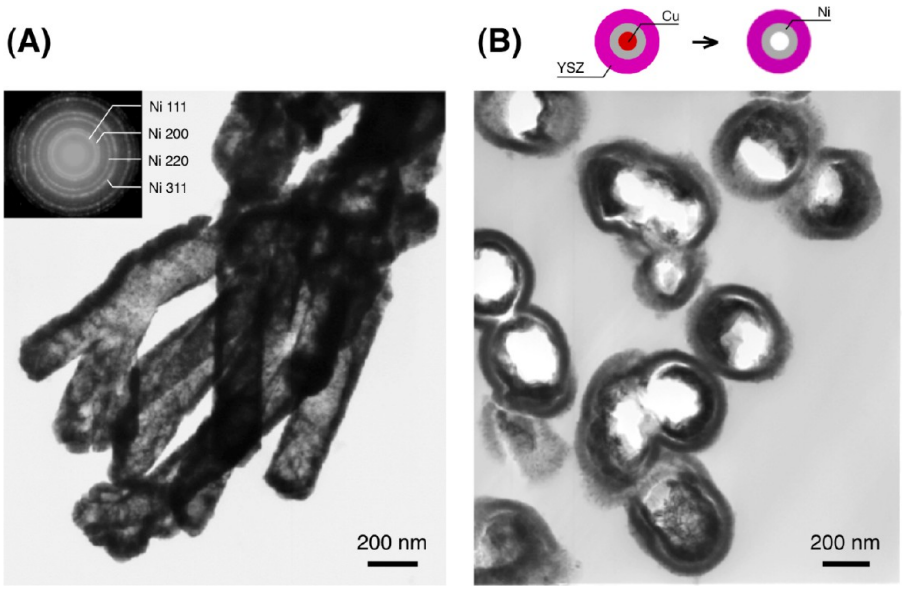

Figure 9. (A) TEM image of Ni hollow tubes created after anodic dissolution of Cu from the core−shell Cu−Ni NWs. (B) Cross-sectional TEM images of Ni−YSZ hollow tubes after anodic dissolution of Cu from the cores.

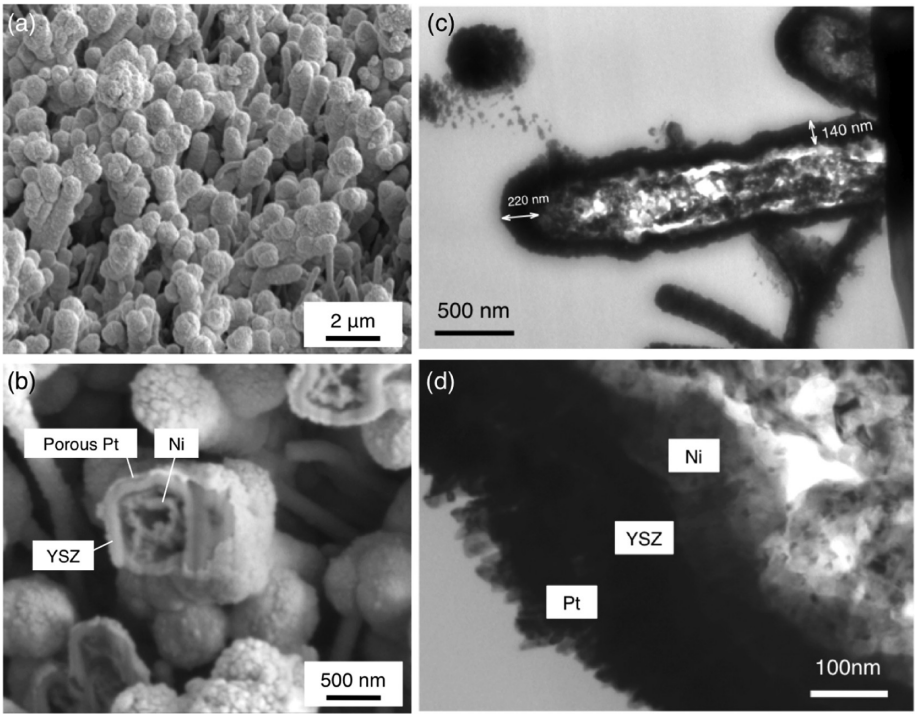

Figure 10. SEM images of (a) porous Pt-coated double-wall Ni−YSZ NT arrays and (b) FIB cut cross sections of multiwall Ni−YSZ−Pt NTs. (c,d) Cross-sectional TEM images in the longitudinal direction of a multiwall Ni−YSZ−Pt NT.

denoted in Figure 11a. The red arrows indicate the binding energy positions for Ni. However, no detectable amount of Ni (less than 1 atom %) is evident at any of these positions, indicating that Ni is completely removed from YSZ NTs. Also, a dominant spectrum for Zr and a less intensive spectrum of Y are observed. Based on the assumption that Y and Zr are incorporated as Y_2O_3 and ZrO_2 into the structure, respectively, the molar fraction of Y_2O_3 in the ZrO_2 matrix film calculated from the intensities is estimated to be 6−7 mol % Y_2O_3 doping in the ZrO_2 matrix film. This Y_2O_3 doping concentration is close to optimum for high ionic conductivity[21] and matches the targeted value we programmed for ALD process control. We had already demonstrated that these ALD films serve as excellent solid electrolyte films for SOFCs in previous work.[10−12] The spectrum of Cu near 8.0 eV in Figure 11c is due to the Cu TEM grid used. Furthermore, the

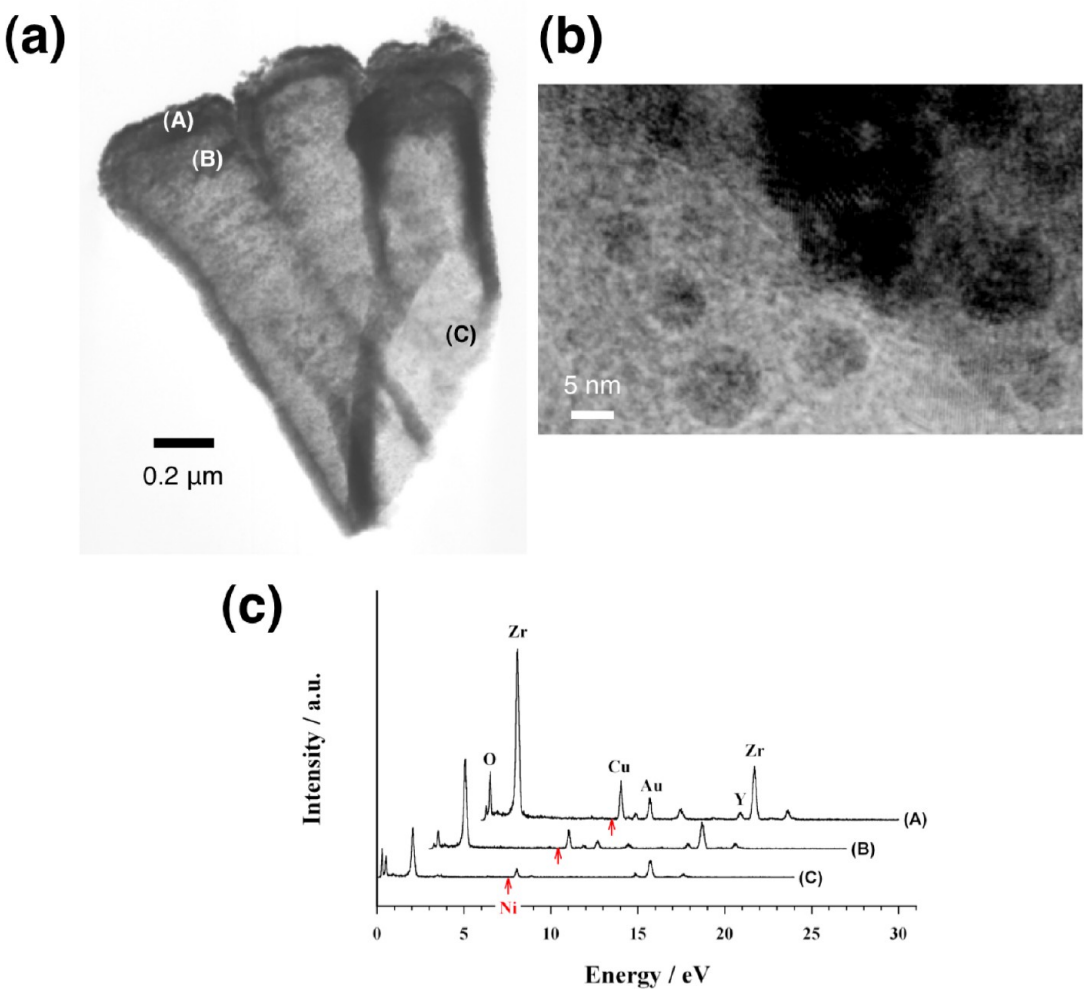

Figure 11. (a,b) TEM images of YSZ hollow tubes. (c) EDS spectra from local positions denoted by (A), (B), and (C) in the image (a).

spectrum of Au is the result of a residue from the thin sputter-coated Au layer that is needed for SEM observations carried out before the TEM analyses. For this reason, Au is detected particularly near the tips (A and B).

Cross-sectional image of the double-wall Ni−YSZ NT is shown in Figure 12A, while the EDS spectra from the (A) inner and (B) outer walls are presented, respectively, in Figure 12B. In the spectra from the inner wall, intensities for Ni near 0.9 and 7.5 eV are dominantly high while Zr spectra near 2.0 and 15.7 eV are significantly smaller as contrasted. We must note that the TEM grid used for this observation is made of Au, different from the observations in Figure 11. Consequently, Cu is significantly etched out from the core, albeit a small Cu peak near 8.0 eV suggests incomplete removal. On the other hand, Zr and O peaks are predominant at the outer wall spectrum, where a small peak for Y is visible near 14.9 eV. More importantly, the spectra for Ni have almost disappeared, indicating complete removal. Electron diffraction shows co-presence of Ni and cubic ZrO_2 (c-ZrO_2). Also, no clear evidence of a tetragonal ZrO_2 phase was found.

The inner peripheries of Ni walls have rough surfaces. In ref 22, complicated boundary lines between Cu-rich and Ni-rich regions are delineated in NW cross sections. Additionally, Ni surfaces in contact with an electrolyte become significantly oxidized during anodic dissolution of Cu. Amorphous-like NiO*x* may then grow in inner periphery regions.

Fuel Cell Behavior of NT-SOFC. Figure 13 shows top SEM views of flat and NT MEAs after being heated at 550 °C. The flat MEA produced critical cracks as indicated by the arrow due to thermal strains. The free-standing region is the central circular area with a diameter of approximately 1.5 mm in Figure 13. In contrast, the NT MEA retains its free-standing structure even after being heated at 550 °C during fuel cell measurements as presented below.

The fuel cell performance of the NT MEA array was measured at the intermediate temperature of 550 °C using H_2 as the fuel and ambient air on the Pt cathode side. Figure 14 shows fuel cell voltages generated by the NT-SOFC as a function of current density at H_2 flow rates of 10, 20, and 60 sccm. An open circuit voltage

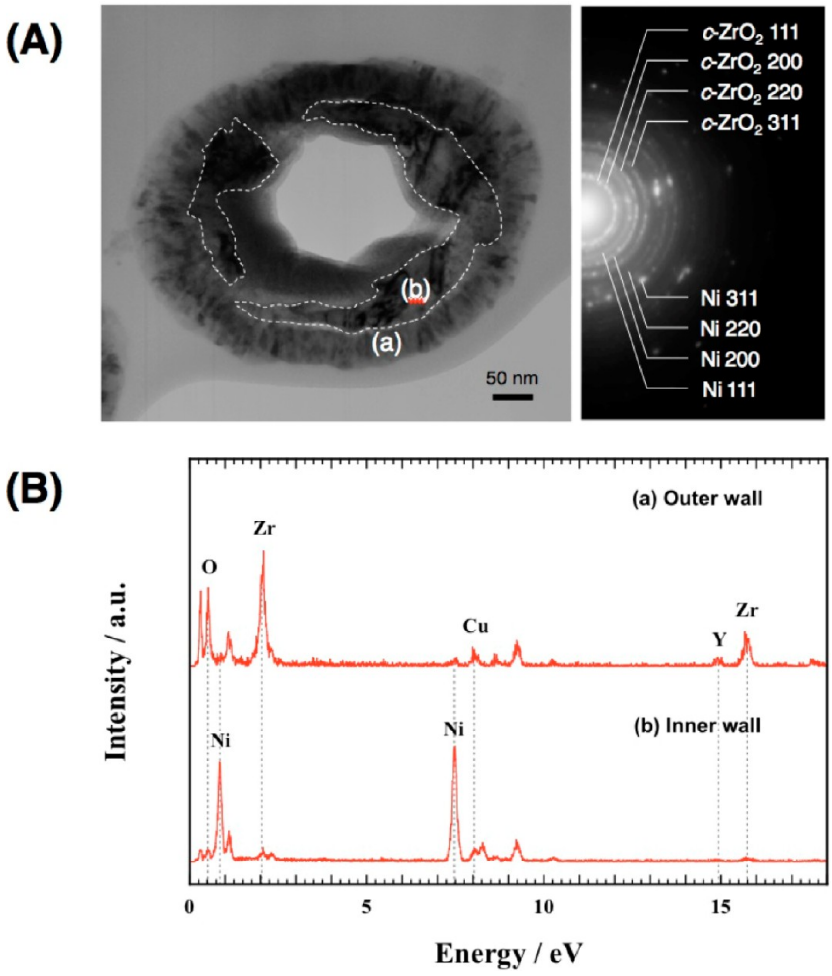

Figure 12. (A) Cross-sectional TEM image of a double-wall Ni−YSZ NT (the inner and outer walls are separated with the dotted lines) and its electron diffraction pattern. (B) EDS spectra from (a) the inner YSZ wall and (b) outer Ni wall in (A).

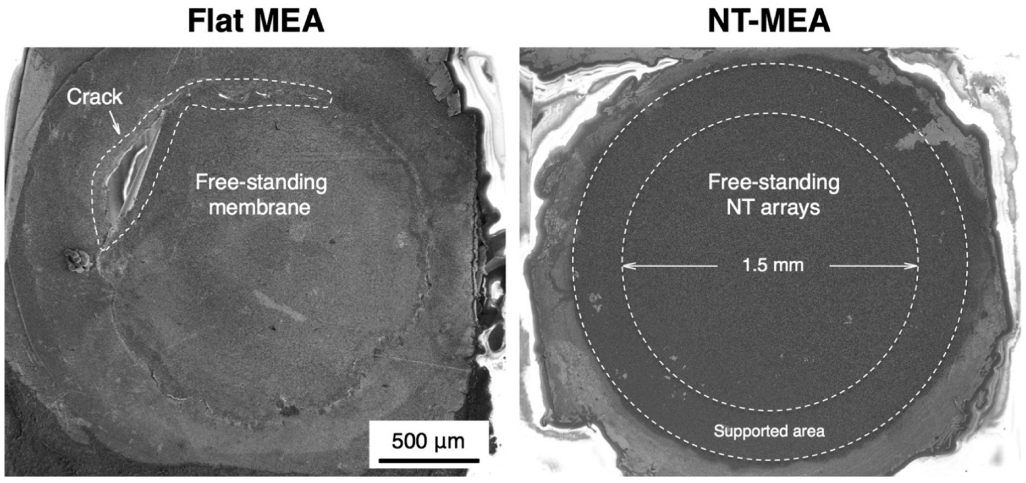

Figure 13. SEM images of flat and NT MEAs. The arrow indicates a hole created by crack of a free-standing membrane due to thermal strains. The inner dotted line circle indicates the free-standing NT array region sustained by the peripheral supported area.

(OCV) of approximately 660 mV is successfully obtained with a 10 sccm H_2 flow rate. The maximum power density is about 1.0 μW cm^{-2} under this condition. However, as the H_2 flow rate is increased, the OCV gradually decreased to 500 mV at 60 sccm, while the current density increased with the H_2 flow rate. The resulting power density also increased with the H_2 flow rate.

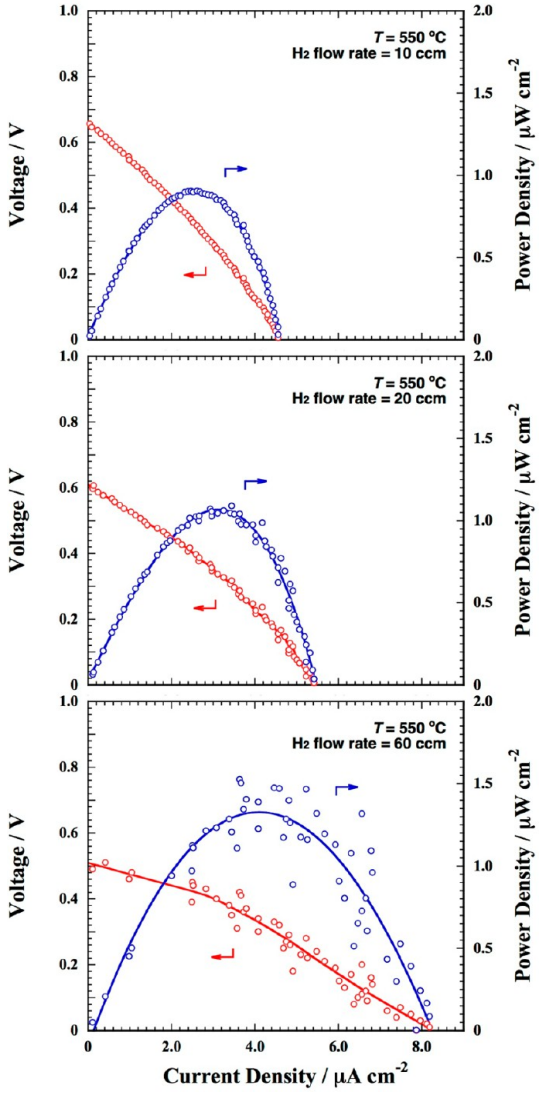

Figure 14. Voltage–current–power density (*V*–*I*–*P*) plots the NT-SOFC array operating at 550 °C with H_2 flow rates of 10, 20, and 60 sccm.

Table 1 summarizes the measurement results of fuel cell performances of a flat MEA and a NT MEA at 550 °C. A flat MEA was not able to retain its own free-standing structure at 550 °C. It was critically broken by cracks during heating. On the other hand, a NT MEA indicated stable OCV and did not yield visible cracks. It is conceivable that strains due to expansion of free-standing NTs are accommodated by the free spaces in the NT array structure.

It is obvious from the low OCV values that there is likely chemical shorting between the fuel side and the air side compartments possibly due to cracks or defective MEA tubes. The observed flow rate dependence of the OCV supports the possibility of chemical shorting as described above. It is possible that lower OCV values observed at higher H_2 flow rates may be the result of chemical shorting between the fuel and air compartments through gas leaks across some of the

TABLE 1. Comparison in Fuel Cell Performance between a Flat MEA and a NT MEA

NT height	condition at 550 °C	OCV	max power density
0 μm	cracked	<5 mV	0
~5 μm	stable	500–700 mV	1.0–1.5 μW cm^{-2}

imperfectly capped defective NTs or nanocracks. The dependence of the observed current on H_2 flow rate suggests also diffusional limitations in the gas phase and raises questions if H_2 is properly and uniformly supplied to all NTs in the array. It is also quite likely that the low power (or current) density is due to nonuniform or incomplete surface coverage of the Pt and Ni electrodes, resulting in inefficient use of the total available surface area of the MEA array. Both of these factors most likely play a major role in the rather poor cell performance of the MEA array.

Clearly, sufficiently high power densities or cell performance are not yet achieved in this work. Optimization of the fabrication process to ensure gastight and complete NTs with uniformly layered porous electrodes still requires further investigation. However, the preliminary results of this study are encouraging and present new opportunities in miniaturizing SOFCs for low to intermediate temperature operation. This study introduces a unique technique for porous Ni fabrication on the inner walls of NT MEAs. Since the ALD process is surface-limited, it offers conformal layers of uniform thickness, which is a desirable quality for coating or covering 3-D structures with ultrathin films. Moreover, ALD is able to deliver precursor molecules to narrow spaces like interiors of closed-end NTs. This allows opportunities to explore a range of materials or even two-phase cermets toward a superior anode on the inner NT wall, in place of Ni. Work is still underway in our laboratory to optimize the fabrication methodology and processing to ultimately make operational NT-SOFC MEAs of superior performance.

CONCLUSIONS

The present study is a prelude to the development of extremely high surface area ultrathin NT fuel cell arrays and reports the successful demonstration of a multiwall Ni/YSZ/Pt NT-SOFC. It also introduces a template-based methodology for the fabrication of multiwall NT MEA array structures. Using this methodology, approximately 20-fold increase in the effective surface area was achieved. Model predictions for a 10 μm thick template membrane indicate, however, that up to 40-fold enhancement can be attained, while even higher enhancement values are potentially possible when thicker membranes are employed for templating. Fuel cell behavior of the NT-SOFC array was successfully demonstrated, although the cell performance

was poor. Nevertheless, the encouraging results achieved in this study pave the way toward fabrication of high-performance low-temperature functional micro-SOFCs.

METHODS

Electrodeposition of Ni and Ni−Cu NW Arrays. Ni and Ni−Cu were electrodeposited into the pores of polycarbonate membranes. For Ni electrodeposition, an aqueous electrolyte containing 1.0 M $NiSO_4$, 0.19 M $NiCl_2$, and 0.62 M H_3BO_3 at pH 3.4 was used. For Ni−Cu electrodeposition, an aqueous electrolyte containing 0.05 M $CuSO_4$, 0.4 M $Ni(SO_3NH_2)_2$, and 0.6 M H_3BO_3 was used. The counter electrode was a Ni sheet, and a Ni wire with a diameter of 1.0 mm was employed as the reference electrode. The effective surface of the Ni wire reference electrode was localized at the tip only, by insulating the rest of the wire. The tip of the reference electrode was placed 2.0 mm away from the template membrane face. A constant potential of −1.0 V with respect to a Ni reference electrode was applied during electrodeposition. Ni NWs typically propagated to the other ends of pores after 200−220 s of electrodeposition. Hence, electrodeposition was terminated after 150 s, and the polycarbonate template membrane was dissolved in dichloromethane, exposing Ni NWs.

ALD. A YSZ film of 50 nm in thickness was grown conformally on NW surfaces by ALD. The details of the ALD instrument used in this work was previously described elsewhere.[10] Precursors used for ZrO_2 and Y_2O_3 deposition were tetrakis(dimethylamido)-zirconium $[Zr(NMe_2)_4]$ and tris(methylcyclopentadienyl)yttrium $[Y(MeCp)_3]$, respectively. Water vapor was used as the oxidant. One ALD cycle is composed of individual pulses of precursors $[Zr(NMe_2)_4$ or $Y(MeCp)_3]$, argon, water vapor, and argon in a sequential manner. Argon pulse is used for purging the ALD chamber. The substrate temperature was set at 250 °C during ALD growth. For doping, one ALD cycle for Y_2O_3 was introduced after every seven ALD cycles of ZrO_2.

YSZ NTs. After ALD growth of the YSZ film, electrodeposited NWs were dissolved to create hollow interiors in YSZ-coated NW arrays. To dissolve Ni NWs, a 10 vol % HNO_3 solution at room temperature was used. For Ni−Cu NWs, anodic dissolution of Cu cores was achieved in a solution of 1.2 M $Ni(H_2NSO_3)_2$ and 0.6 M H_3BO_3. A constant potential of +1.0 V with respect to a reference Cu wire electrode was applied until anodic current reached a saturation value close to zero.

Fuel Cell Test. We employed our homemade fuel cell test station that has been used previously for free-standing thin film SOFCs.[10−12] A fabricated MEA sample was placed on the periphery of a vertically standing tubular furnace with the center hole of less than 1.0 cm in diameter. A H_2 delivery pipeline penetrates the furnace in the horizontal direction, whereby the primary H_2 flow direction is normal to the NT longitudinal direction and passes through under the NT-MEA sample. H_2 gas diffuses to the bottom of MEA from below. A metal ring with the same size as the furnace was mounted onto an MEA sample placed on the furnace. The top ring was screwed down at four positions to eliminate spaces between the sample and the furnace edges. The detail of the fuel cell test system is found elsewhere.[10]

Conflict of Interest: The authors declare no competing financial interest.

Acknowledgment. T.M.G. and F.B.P. gratefully acknowledge partial support from the Center on Nanostructuring for Efficient Energy Conversion (CNEEC) at Stanford University, an Energy Frontier Research Center funded by the U.S. Department of Energy, Office of Science, Office of Basic Energy Sciences under Award Number DE-SC0001060.

REFERENCES AND NOTES

1. Whitney, T. M.; Jiang, J. S.; Searson, P. C.; Chien, C. L. Fabrication and Magnetic Properties of Arrays of Metallic Nanowires. *Science* **1993**, *261*, 1316–1319.
2. Martin, C. R. Nanomaterials: A Membrane-Based Synthetic Approach. *Science* **1994**, *266*, 1961–1966.
3. Kelzenberg, M. D.; Boettcher, S. W.; Petykiewicz, J. A.; Turner-Evans, D. B.; Putnam, M. C.; Warren, E. L.; Spurgeon, J. M.; Briggs, R. M.; Lewis, N. S.; Atwater, H. A. Enhanced Absorption and Carrier Collection in Si Wire Arrays for Photovoltaic Applications. *Nat. Mater.* **2010**, *9*, 239–244.
4. Taberna, P. L.; Mitra, S.; Poizot, P.; Simon, P.; Tarascon, J.-M. High Rate Capabilities Fe_3O_4-Based Cu Nano-Architectured Electrodes for Lithium-Ion Battery Applications. *Nat. Mater.* **2006**, *5*, 567–573.
5. Cheah, S. K.; Perre, E.; Rooth, M.; Fondell, M.; Hårsta, A.; Nyholm, L.; Boman, M.; Gustafsson, T.; Lu, J.; Simon, P.; *et al.* Self-Supported Three-Dimensional Nanoelectrodes for Microbattery Applications. *Nano Lett.* **2009**, *9*, 3230–3233.
6. Xu, C.; Wang, H.; Shen, P. K.; Jiang, S. P. Highly Ordered Pd Nanowire Arrays as Effective Electrocatalysts for Ethanol Oxidation in Direct Alcohol Fuel Cells. *Adv. Mater.* **2007**, *19*, 4256–4259.
7. Zhong, Y.; Xu, C.-L.; Kong, L.-B.; Li, H.-L. Synthesis and High Catalytic Properties of Mesoporous Pt Nanowire Array by Novel Conjunct Template Method. *Appl. Surf. Sci.* **2008**, *255*, 3388–3393.
8. Choi, S. M.; Kim, J. H.; Jung, J. Y.; Yoon, E. Y.; Kim, W. B. Pt Nanowires Prepared *via* a Polymer Template Method: Its Promise toward High Pt-Loaded Electrocatalysts for Methanol Oxidation. *Electrochim. Acta* **2008**, *53*, 5804–5811.
9. Zhang, X.; Lu, W.; Da, J.; Wang, H.; Zhao, D.; Webley, P. A. Porous Platinum Nanowire Arrays for Direct Ethanol Fuel Cell Applications. *Chem. Commun.* **2009**, 195–197.
10. Shim, J. H.; Gür, T. M.; Prinz, F. B. Proton Conduction in Thin Film Yttrium-Doped Barium Zirconate. *Appl. Phys. Lett.* **2008**, *92*, 253115.
11. Su, P.-C.; Chao, C.-C.; Shim, J.-H.; Fasching, R.; Prinz, F. B. Solid Oxide Fuel Cell with Corrugated Thin Film Electrolyte. *Nano Lett.* **2008**, *8*, 2289–2292.
12. Chao, C.-C.; Hsu, C.-M.; Cui, Y.; Prinz, F. B. Improved Solid Oxide Fuel Cell Performance with Nanostructured Electrolytes. *ACS Nano* **2011**, *5*, 5692–5696.
13. Avrami, M. Kinetics of Phase Change I: General Theory. *J. Chem. Phys.* **1939**, *7*, 1103–1112.
14. Avrami, M. Granulation, Phase Change, and Microstructure: Kinetics of Phase Change. III. *J. Chem. Phys.* **1941**, *9*, 177–184.
15. Motoyama, M.; Fukunaka, Y.; Sakka, T.; Ogata, Y. H.; Kikuchi, S. Electrochemical Processing of Cu and Ni Nanowire Arrays. *J. Electroanal. Chem.* **2005**, *584*, 84–91.
16. Schönenberger, C.; van der Zande, B. M. I.; Fokkink, L. G. J.; Henny, M.; Schmid, C.; Kruüger, M.; Bachtold, A.; Huber, R.; Birk, H.; Staufer, U. Template Synthesis of Nanowires in Porous Polycarbonate Membranes: Electrochemistry and Morphology. *J. Phys. Chem. B* **1997**, *101*, 5497–5505.
17. Petzow, G. *Metallographic Etching*, 2nd ed.; ASM International: Materials Park, OH, 1999.
18. Thompson, C. V. Grain Growth in Thin Films. *Annu. Rev. Mater. Sci.* **1990**, *20*, 245–268.
19. Wang, Q.; Wang, G.; Han, X.; Wang, X.; Hou, J. Controllable Template Synthesis of Ni/Cu Nanocable and Ni Nanotube Arrays: A One-Step Coelectrodeposition and Electrochemical Etching Method. *J. Phys. Chem. B* **2005**, *109*, 23326–23329.
20. Liu, Z.; Xia, G.; Zhu, F.; Kim, S.; Markovic, N.; Chien, C.-L.; Searson, P. Exploiting Finite Size Effects in a Novel Core/Shell Microstructure. *J. Appl. Phys.* **2008**, *103*, 64313.
21. Filal, M.; Petot, C.; Mokchah, M.; Chateau, C.; Carpentier, J. L. Ionic Conductivity of Yttrium-Doped Zirconia and the "Composite Effect". *Solid State Ionics* **1995**, *80*, 27–35.
22. Liu, Z.; Elbert, D.; Chien, C.-L.; Searson, P. C. FIB/TEM Characterization of the Composition and Structure of Core/Shell Cu−Ni Nanowires. *Nano Lett.* **2008**, *8*, 2166–2170.